Applied Physics Letters

Silicon photodetector for integrated lithium niobate photonics

Cite as: Appl. Phys. Lett. **115**, 121108 (2019); https://doi.org/10.1063/1.5118901
Submitted: 05 July 2019 . Accepted: 06 September 2019 . Published Online: 20 September 2019

Boris Desiatov, and Marko Lončar

Applied Physics Letters ARTICLE scitation.org/journal/apl

Silicon photodetector for integrated lithium niobate photonics

Cite as: Appl. Phys. Lett. **115**, 121108 (2019); doi: 10.1063/1.5118901
Submitted: 5 July 2019 · Accepted: 6 September 2019 ·
Published Online: 20 September 2019

Boris Desiatov and Marko Lončar[a)]

AFFILIATIONS

J. A. Paulson School of Engineering and Applied Sciences, Harvard University, Cambridge, Massachusetts 02138, USA

[a)]loncar@seas.harvard.edu

ABSTRACT

We demonstrate the integration of an amorphous silicon photodetector with a thin film lithium niobate photonic platform operating in the visible wavelength range. We present the details of the design, fabrication, integration, and experimental characterization of this metal-semiconductor-metal photodetector that features a responsivity of 22 mA/W to 37 mA/W over the wide optical bandwidth spanning in the 635 nm–850 nm wavelength range.

Integration of various photonic components on a single chip, including light sources and detectors, is a critical route toward the realization of dense photonic integrated circuits (PICs).[1] These are of interest not only for traditional applications in data- and telecommunications but also for applications in imaging, metrology, biosensing, nanomedicine, and quantum optics which typically require operation in the visible wavelength range.[2,3] For decades, lithium niobate (LN) has been considered to be an optimum optical material due to its large second order (χ^2) electro-optic coefficient and excellent wideband optical transparency (400 nm–4000 nm). However, traditional LN photonic structures, created by ion exchange or metal in-diffusion, suffer from the low refractive index contrast, resulting in a large cross section of the photonic structures, thus making the dense integration difficult. Recently, thin film lithium niobate on insulator (LNOI) substrates[4] has become commercially available, which combined with advances in nanofabrication has enabled the realization of ultralow loss waveguides (WGs) and high-performance electro-optical (EO) devices both at telecom[5,6] and visible wavelengths.[7] Integration of photodetectors (and eventually laser sources) with a LNOI photonic platform is an important, and currently missing, step that could lead to the implementation of complex functionalities[8] using this emerging PIC platform. Indeed, opportunities offered by the integration of detectors with lithium niobate have been explored before[9,10] albeit using traditional, bulk crystal based, in-diffused LN waveguides with low optical confinement and large mode size. This results, among other things, in a large detector area, thus limiting the response time of the photodetector. In this paper, we demonstrate the monolithic integration of a broadband Metal-Semiconductor-Metal (MSM) photodetector for visible wavelengths in a thin film LNOI photonic platform.

Over the past decade, significant advances have been made along the lines of integration of semiconductor photodetectors with photonics platforms operating in the visible wavelength range, motivated by envisioned applications in biosensing and imaging.[11–15] Compared to PN or PIN junction-based photodetectors used in these experiments, the MSM[16,17] junction-based photodetector described in this work is relatively simple to implement since it does not require dopant implantation.[16,17] Still, MSM photodetectors can have a high responsivity, low capacitance, low dark current, and high operation speed comparable to, and even better than, those of modern PN or PIN photodetectors.[16,17] Previously, such a type of a-Si photodetector at visible wavelengths was demonstrated[18] in sputtered glass waveguides back in 1988. A schematic of our integrated MSM photodetector is shown in Fig. 1. It consists of a thin layer of amorphous silicon (a-Si) deposited on top of the LN waveguide, with a pair of gold electrodes on top of it. Photons at visible wavelengths, propagating down the LN waveguide, are absorbed in the a-Si layer, and generated electron-hole pairs are separated by voltage applied across the MSM junction, giving rise to a photocurrent.

The most important parameter which directly affects the performance of the proposed photodetector is a thickness of the a-Si absorption layer. A very thick a-Si layer ensures that all the optical power propagating in the waveguide is effectively absorbed, but the transport and collection of generated photocarriers become more challenging due to recombination processes. On the other hand, if a very thin layer

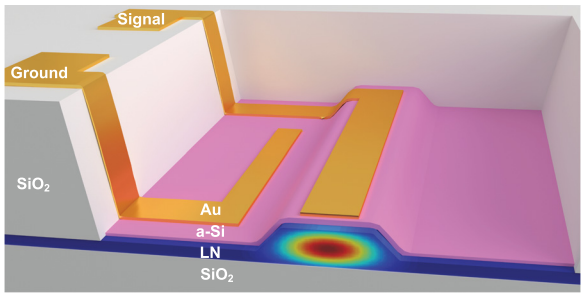

FIG. 1. An illustration of the integrated photodetector device consisting of the LN waveguide with a cross section of $800 \times 300\,\text{nm}^2$, an amorphous silicon (a-Si) absorption layer, and gold contacts.

of a-Si is used, the optical field can have significant overlap with metal electrodes which may result in unwanted Ohmic losses. However, it is important to note that the interaction of optical energy with a metal contact can also contribute to the generation of electron-hole pairs due to the internal photoemission effect[19,20] (generation of hot carriers).

Our rib LN waveguide has a dimension of $800 \times 300\,\text{nm}^2$ and can support both fundamental transverse electric (TE) and transverse magnetic (TM) modes as shown in Figs. 2(a) and 2(c), respectively. The corresponding TE and TM modes of the photodetector structure are shown in Figs. 2(b) and 2(d) respectively. In order to find an optimal thickness of the absorption a-Si layer, we have performed a detailed study of the optical absorption length and parasitic Ohmic loss in the metal as a function of the a-Si layer thickness, for both polarizations of interest. Using a 3-dimensional (3D) finite-difference time-domain method simulation (Lumerical, Inc.), we calculated the total absorption length (defined as the distance where the incident power drops to 1/e) and a contribution of optical absorption in the metal (due to Ohmic losses) for several a-Si layer thicknesses, for both fundamental TE and TM modes at a wavelength of 635 nm. The permittivity of the gold material is based on data from Johnson and Christy.[21] The simulated results are summarized in Figs. 2(e) and 2(f), respectively. For a thickness of a-Si below 50 nm, both TE and TM modes have a very high metal loss (more than 50%), making such a thin semiconductor layer ineffective for the realization of the MSM detector. For the TE mode and moderately thick semiconductor layer (above 100 nm), the optical absorption in the metal region can be neglected (less that 5%), and the total absorption length was found to be below 10 μm. For the TM mode, the loss in the metal region of the detector was found to be relatively high (~10%) even for a relatively thick a-Si layer of 300 nm. Such a large difference in the metal-induced optical losses in the cases of TE and TM modes can be explained by different boundary conditions at the semiconductor—metal interface. We choose to work with a 100 nm thick a-Si layer and have calculated the coupling efficiency between the low-loss LN waveguide and a photodetector to be 89%. A cross-sectional side view of optical simulations for the optimal parameters is shown in Fig. 2(g). The reflected and scattered amounts of optical power were found to be 7% and 4%, respectively. These numbers can be further decreased by introducing an adiabatic tapering transition section between the LN waveguide and the photodetector. The absorption length of the photodetector was found to be 6 μm.

The electrical bandwidth of the MSM photodetector can be limited by the capacitance of the electrodes: $C = \varepsilon_0 \varepsilon_{aSi} \frac{Lt}{d}$ or by carrier

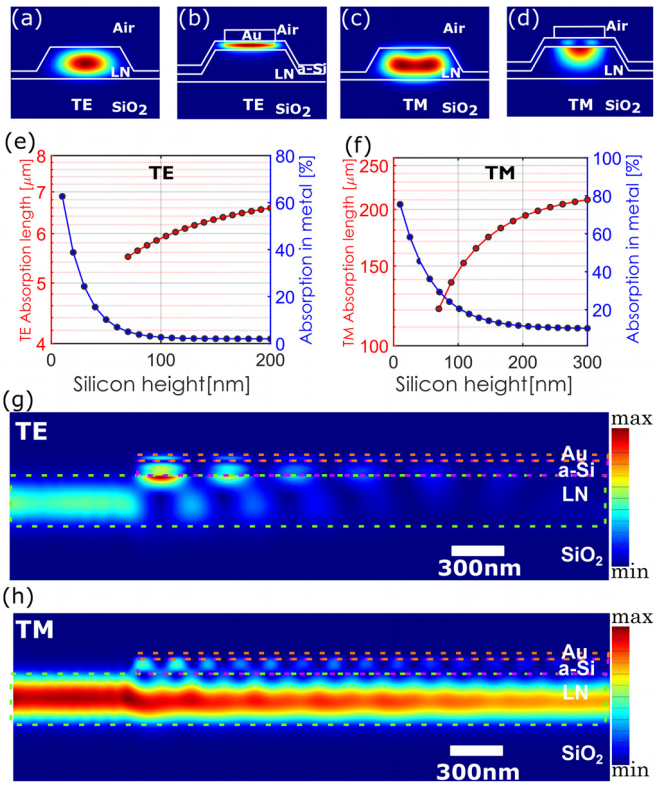

FIG. 2. (a)–(d) Simulated TE and TM optical modes of the LN waveguide and integrated photodetector (thickness of the a-Si layer, 50 nm), respectively. (e) and (f) Simulated coupling length and total amount of optical absorption in the metal vs thickness of the a-Si layer for TE and TM modes, respectively. (g) and (h) Finite difference time domain simulation of the electric field intensity $|E|^2$ in the coupling section for TE and TM polarizations, respectively. Green, purple, and orange lines represent the boundaries of the LN waveguide, a-Si layer, and gold contact, respectively.

collection time[22] $\tau_{collect} = \frac{d}{v_{sat\_aSi}}$. Here, ε_0 is the vacuum dielectric constant, ε_{aSi} the relative dielectric constant, v_{sat_aSi} the a-Si carrier saturation velocity, L the photodetector length, d the distance between the electrodes, and t the photodetector thickness. For a 1 μm distance between the electrodes, the capacitance of the photodetector was calculated to be 0.5 fF, resulting in a RC time constant of 25 ps (for 50 Ω load). The saturation velocity of the a-Si layer strongly depends on deposition/annealing parameters used during the fabrication process. Here, we assume the carrier collection time of our detector to be on the order of nanosecond, based on the previously reported value for the saturation drift velocity of 8.5×10^5 cm/V^2 (Ref. 23) (and taking into account the detector geometry).This value of carrier collection time in our a-Si MSM photodetectors is similar to the values previously reported.[24]

Our devices were fabricated on LN-on-insulator (LNOI) chips with a 300 nm X-cut LN layer on top of the 2-μm thick thermally grown silicon dioxide layer (NanoLN). First, the photonic structures were defined in electron-beam resist by using an electron beam lithography tool (Elionix), and then, the pattern was transferred into the LN layer by using the Ar+ plasma based reactive ion etching (RIE) tool

(etch depth of 250 nm). Next, the devices were covered by a 1-μm silicon dioxide layer by using the plasma-enhanced chemical vapor deposition (PECVD) tool (for optical and electrical insulation), and detector areas were opened by using the optical photolithography step followed by the RIE of silicon dioxide. Next, the absorption layer of p-doped a-Si was deposited on top of the photonic devices using PECVD followed by a rapid thermal processing (RTP). Next, a-Si was patterned and removed from the chip except the active areas of the photodetector by using the additional photolithography step and RIE. Finally, gold electrodes were formed by using photolithography and the metal lift-off process. After the fabrication, the waveguide facets were diced and polished. A false-color scanning electron microscopy (SEM image of the fabricated device is shown in Fig. 3). The detectors are 6 μm long. The LN waveguide cross section is $800 \times 300\ \text{nm}^2$, and the electrodes are 2 μm wide, with 1 μm spacing between them.

In order to experimentally characterize the photoelectric response of our detectors, we coupled a TE polarized 635 nm light (from the tunable new focus velocity laser) into our waveguide. The end-fire coupling technique with a lensed fiber with 1 μm spot size (Oz Optics) was used. The coupling efficiency was estimated to be 10 dB/facet. We note that this can be significantly improved using recently demonstrated spot-size converters.[25] The propagation waveguide loss was estimated to be 0.6 dB/cm by measuring the quality factor of a reference microring resonator fabricated on the same chip ($Q \sim 400\,000$). Next, we measured an I-V characteristic of the integrated photodetector (SMU Keithley 2400) for different in-coupled optical powers, as shown in Fig. 4(a). The responsivity of the integrated photodetector was found to be 22 mA/W at 635 nm wavelength, with a dark current of 0.1 nA. This value is comparable to the previously reported values[18,26] in the case of integrated-Si photodetectors. It should be noticed that while the responsivity of our a-Si detector is about an order of magnitude lower than commercial Si and InGaAs detectors [$R(630\,\text{nm}) = 0.5$ A/W $R(630\,\text{nm}) = 0.2$ A/W, respectively], our approach offers the important advantages of simplicity and on-chip integration with the LN platform. Finally, we measured a responsivity of the photodetector as a function of a wavelength in 720–850 nm range using a M2 SolsTis tunable laser. Figure 4(b) shows

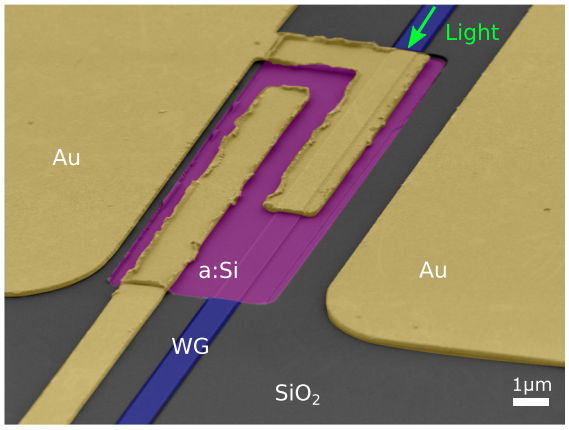

FIG. 3. False colored SEM image of the a-Si layer integrated with the LN waveguide (WG). Gold, pink, and violet colors represent the metal contacts, a-Si layer, and LN waveguide under the silicon dioxide cladding, respectively.

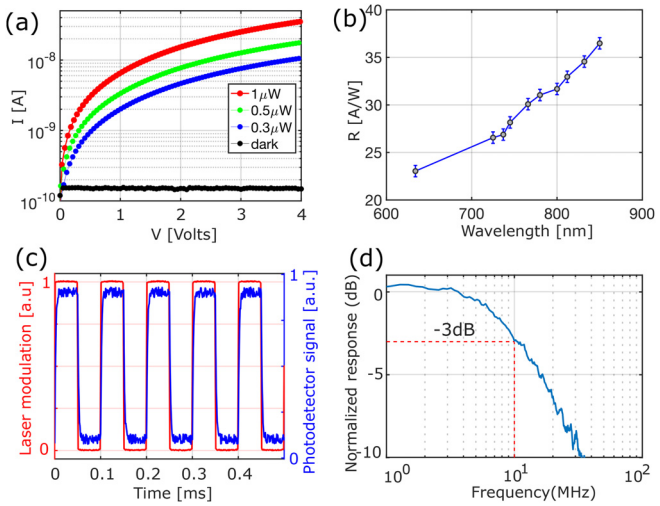

FIG. 4. Experimental characterization of the a-Si MSM photodetector. (a) IV response measured at a wavelength of 635 nm for different optical powers inside the waveguide. (b) Responsivity as a function of wavelength, at −0.5 V bias. (c) Temporal response for an input optical square wave signal at 1 kHz. (d) Normalized frequency response of the integrated photodetector shows a 3 dB roll-off frequency at 10 MHz, limited by the performance of the transimpedance amplifier (TIA). The red line indicates the −3 dB threshold of TIA.

an average spectral response of 5 different detectors over this wide wavelength range, and the error bars represent the standard deviation from the average. The maximum responsivity of 37 mA/W was achieved at a wavelength of 850 nm. This is expected since the responsivity of a photodiode (PN, PIN, or MSM) typically increases at longer wavelengths according to $\Re = \eta \frac{e}{h\upsilon}$, where $h\upsilon$ is the photon energy, η is the quantum efficiency, and e is the elementary charge. At the longer wavelengths (above the bandgap of a-Si), we would expect an abrupt decrease in the responsivity. The exact value of the bandgap of a-Si is strongly dependent on deposition conditions and techniques and can be varied between 1 and 3.6 eV.[27,28] To estimate the bandgap of our a-Si, we have fabricated a reference sample by depositing a 1 μm thick film of the a-Si layer on top of the glass quartz substrate. Next, we measured the transmittance spectrum of the a-Si film by using an Agilent Cary 60 UV/VIS spectrophotometer. Finally, using a Tauc plot,[29] we estimate the bandgap of our a-Si to be 1.4 eV. The responsivity of our photodetector is also strongly dependent on the quality of the a-Si layer. Material defects such as morphology imperfection, voids, and grain boundaries can cause unwanted scattering of the light which will decrease the optical absorption and decrease the responsivity.

Next, we evaluated the temporal-response of the a-Si integrated photodetector by directly modulating the tunable laser using the signal at a frequency of 10 kHz. The detected electrical signal from the photodetector was amplified by using a transimpedance amplifier (TIA) (AD8488[30] amplifier with the expected cut-off frequency at 10 MHz) and is displayed on an oscilloscope [Fig. 4(c)]. The electro-optical bandwidth of our detector was measured using the vector network analyzer (VNA). The laser was modulated by VNA, and the detected electrical signal was amplified by TIA. Figure 4(d) shows a normalized (relative to the coaxial cable loss) frequency response of our photodetector with a 3 dB roll of frequency of 10 MHz, limited by the cut-of

frequency of TIA (shown by the red line). Although being low, this bandwidth is sufficient for several on-chip applications of interest, including power monitoring, frequency-modulation spectroscopy,[31] and Pound–Drever–Hall laser-locking technique.[32] By further optimization of the deposition conditions of the a-Si layer or leveraging commercially available polysilicon deposition foundries, it may be possible to realize a high speed (tens of gigahertz) optical integrated a-Si photodetector. For example, such high-speed photodetectors have been previously demonstrated with a hydrogenated a-Si layer.[33,34] This would in turn enable additional applications in visible light communication[35] and ultrafast optical characterization.[36]

Finally, we integrated our a-Si photodetector with a microring resonator device as shown in Fig. 5(a). In this case, the length of the photodetector was chosen to be 5 μm in order to allow for only partial absorption of the optical energy, about 50% in our case. The remaining optical energy was transmitted through the photodetector and was collected by lensed fiber and detected using the commercial photodetector (PDA36A, Thorlabs, responsivity, 0.65 A/W) for comparison measurements. The spectral response of our integrated device was measured using a tunable laser, and the results are shown in Fig. 5(b).

Figure 5(b) shows a transmission spectrum of the fabricated microring resonator measured with both the integrated a-Si photodetector and commercial photodetector. By fitting the experimental result to a Lorentzian function, we estimated a loaded Q factor of the fabricated microring resonator to be 1.5×10^5. The value of

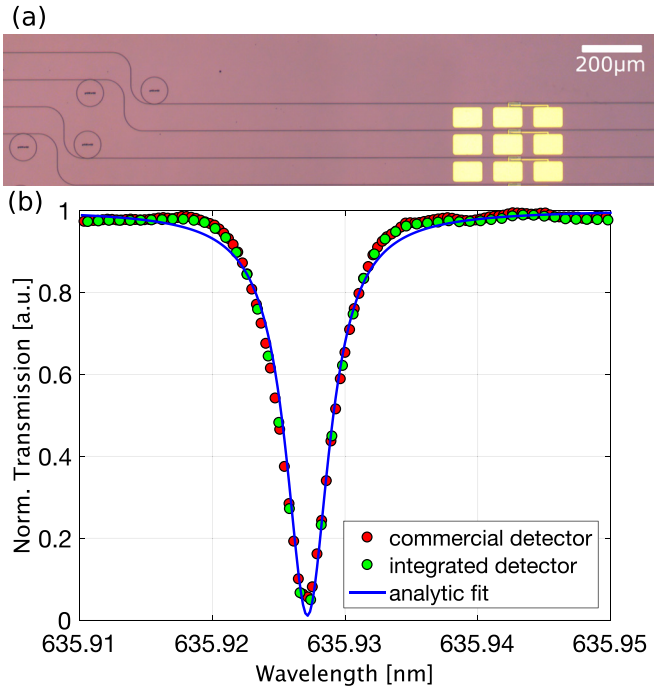

FIG. 5. (a) Optical image of the fabricated a-Si photodetector integrated with a microring cavity. (b) Measured transmission spectrum of integrated LN microring resonators. Red and green dots: Optical signal measured by using the integrated a-Si photodetector and the external commercial Si photodetector, respectively. Blue line: A fit to the Lorentzian function with a loaded Q factor estimated to be 1.5×10^5.

the quality factor is lower than previously reported values[7] due to non-optimized waveguide dimensions and additional high temperature (700 °C) fabrication steps needed to realize the detector[37] including a-Si deposition and rapid thermal processing (RTP). The measured spectral photoresponse of the integrated photodetector is in good agreement with the results obtained using the commercial photodetector. The high spectral selectivity of the integrated photonic device that consists of a microring resonator filter and the a-Si integrated photodetector makes it a good candidate for the realization of a large variety of devices for detection and sensing applications such as integrated spectrometers[38] and biosensors.[11]

In conclusion, we have demonstrated an integrated a-Si photodetector in a LN photonic platform at visible wavelengths. A responsivity of 37 mA/W was measured at a wavelength of 850 nm, which is the primary wavelength for multimode fiber optical communication systems based on the Vertical-Cavity Surface Emitting Laser (VCSEL). The operating bandwidth of the integrated photodetector was measured to be 10 MHz, limited by using the transimpedance amplifier we used. Additionally, we have demonstrated wavelength selective detection by monolithically integrating the photodetector with a microring resonator with a quality factor of 150 000. Furthermore, using different materials (e.g., germanium) for the absorption layer with different energy bandgaps, it will be possible to enhance the bandwidth of the photodetector toward infrared and mid-infrared spectral windows. Another promising approach for the realization of a broadband and high speed integrated photodetector is to use emerging 2d materials.[5,39] We believe that the integrated LN photonic platform will become a promising candidate for the realization of multielement monolithic photonic circuits.

Lithium niobate devices were fabricated at the Center for Nanoscale Systems (CNS) at Harvard, a member of the National Nanotechnology Infrastructure Network, supported by the NSF under Award No. 1541959.This work was supported in part by the National Science Foundation (NSF) (Nos. ECCS-1740296 E2CDA and IIP-1827720), Defense Advanced Research Projects Agency (DARPA) (No. W31P4Q-15-1-0013), and Air Force Office of Scientific Research (AFOSR) (MURI: No. FA9550-12-1-0389).

REFERENCES

[1]D. Miller, Nat Photonics **4**, 3 (2010).
[2]H. Chen, H. Fu, X. Huang, X. Zhang, T.-H. Yang, J. A. Montes, I. Baranowski, and Y. Zhao, Opt. Express **25**, 31758 (2017).
[3]T.-J. Lu, M. Fanto, H. Choi, P. Thomas, J. Steidle, S. Mouradian, W. Kong, D. Zhu, H. Moon, K. Berggren, J. Kim, M. Soltani, S. Preble, and D. Englund, Opt. Express **26**, 11147 (2018).
[4]P. Rabiei and P. Gunter, Appl. Phys. Lett. **85**, 4603 (2004).
[5]G. Wang, Y. Zhang, C. You, B. Liu, Y. Yang, H. Li, A. Cui, D. Liu, and H. Yan, Infrared Phys. Technol. **88**, 149 (2018).
[6]M. He, M. Xu, Y. Ren, J. Jian, Z. Ruan, Y. Xu, S. Gao, S. Sun, X. Wen, L. Zhou, L. Liu, C. Guo, H. Chen, S. Yu, L. Liu, and X. Cai, Nat. Photonics **13**, 359 (2019).
[7]B. Desiatov, A. Shams-Ansari, M. Zhang, C. Wang, and M. Lončar, Optica **6**, 380 (2019).
[8]R. Hamerly, L. Bernstein, A. Sludds, M. Soljačić, and D. Englund, Phys. Rev. X **9**, 021032 (2019).
[9]W. K. Chan, A. Yi-Yan, T. Gmitter, L. T. Florez, J. L. Jackel, E. Yablonovitch, R. Bhat, and J. P. Harbison, IEEE Trans. Electron Devices **36**, 2627 (1989).
[10]J. P. Höpker, T. Gerrits, A. Lita, S. Krapick, H. Herrmann, R. Ricken, V. Quiring, R. Mirin, S. W. Nam, C. Silberhorn, and T. J. Bartley, APL Photonics **4**, 056103 (2019).
[11]T. Kamei, B. M. Paegel, J. R. Scherer, A. M. Skelley, R. A. Street, and R. A. Mathies, Anal. Chem. **75**(20), 5300–5305 (2003).

[12]A. Jóskowiak, M. S. Santos, D. M. F. Prazeres, V. Chu, and J. P. Conde, Sens. Actuators, B **156**, 662 (2011).
[13]P. Novo, D. M. França Prazeres, V. Chu, and J. P. Conde, Lab Chip **11**, 4063 (2011).
[14]A. Samusenko, V. Hamedan, G. Pucker, M. Ghulinyan, F. Ficorella, R. Guider, D. Gandolfi, and L. Pavesi, in *2015 XVIII AISEM Annual Conference* (IEEE, 2015), pp. 1–4.
[15]M. Moridi, S. Tanner, N. Wyrsch, P.-A. Farine, and S. Rohr, Procedia Chem. **1**, 1367 (2009).
[16]S. M. Sze and K. K. Ng, *Physics of Semiconductor Devices* (Wiley-Interscience, 2007).
[17]P. R. Berger, Proc. SPIE **4285**, 198–207 (2001).
[18]M. M. Howerton and T. E. Batchman, J. Lightwave Technol. **6**, 1854 (1988).
[19]B. Desiatov, I. Goykhman, N. Mazurski, J. Shappir, J. B. J. B. Khurgin, and U. Levy, Optica **2**, 335 (2015).
[20]W. Li and J. G. Valentine, Nanophotonics **6**, 177 (2017).
[21]P. B. Johnson and R. W. Christy, Phys. Rev. B **6**, 4370 (1972).
[22]H. Zimmermann, *Integrated Silicon Optoelectronics* (Springer Berlin Heidelberg, Berlin, Heidelberg, 2000).
[23]R. I. Devlen, E. A. Schiff, J. Tauc, and S. Guha, "Electric Field Dependence of the Electron Drift Velocity in Hydrogenated Amorphous Silicon," in *MRS Proceedings* (Mater. Res. Soc. Proc., 1989), Vol. 149, p. 107.
[24]A. M. Johnson, A. M. Glass, D. H. Olson, W. M. Simpson, and J. P. Harbison, Appl. Phys. Lett. **44**, 450 (1984).
[25]A. Shams-Ansari, C. Wang, L. He, L. Marko, M. Zhang, and R. Zhu, Opt. Lett. **44**(9), 2314–2317 (2019).
[26]A. Samusenko, V. J. Hamedan, G. Pucker, M. Ghulinyan, F. Ficorella, R. Guider, D. Gandolfi, and L. Pavesi, in *2015 XVIII AISEM Annual Conference* (IEEE, 2015), pp. 1–4.
[27]R. H. Klazes, M. H. L. M. van den Broek, J. Bezemer, and S. Radelaar, Philos. Mag. B **45**, 377 (1982).
[28]Jasruddin, W. W. Wenas, T. Winata, and M. Barmawi, in *2000 IEEE International Conference on Semiconductor Electronics Proceedings (ICSE 2000) (Cat. No. 00EX425)* (IEEE, 2000), pp. 245–248.
[29]J. Tauc, Mater. Res. Bull. **3**, 37 (1968).
[30]Z.-C. Zeng and Z. D. Schultz, Rev. Sci. Instrum. **89**, 083105 (2018).
[31]G. C. Bjorklund, M. D. Levenson, W. Lenth, and C. Ortiz, Appl. Phys. B: Photophys. Laser Chem. **32**, 145 (1983).
[32]R. W. P. Drever, J. L. Hall, F. V. Kowalski, J. Hough, G. M. Ford, A. J. Munley, and H. Ward, Appl. Phys. B: Photophys. Laser Chem. **31**, 97 (1983).
[33]D. R. Larson and R. J. Phelan, Jr., Proc. SPIE **0835**, 59 (1988).
[34]D. H. Auston, P. Lavallard, N. Sol, and D. Kaplan, Appl. Phys. Lett. **36**, 66 (1980).
[35]T.-C. Wu, Y.-C. Chi, H.-Y. Wang, C.-T. Tsai, Y.-F. Huang, and G.-R. Lin, Sci. Rep. **7**, 11 (2017).
[36]D. H. Auston, Appl. Phys. Lett. **26**, 101 (1975).
[37]D. Sugak, I. Syvorotka, O. Buryy, U. Yachnevych, I. Solskii, N. Martynyuk, Y. Suhak, G. Singh, V. Janyani, and S. Ubizskii, IOP Conf. Ser. Mater. Sci. Eng. **169**, 012019 (2017).
[38]X. Ma, M. Li, and J.-J. He, IEEE Photonics J. **5**, 6600807 (2013).
[39]G. Konstantatos, Nat. Commun. **9**, 5266 (2018).